Exploring behaviors of electrode-driven Si quantum dot systems: From charge control to qubit operation

- Supporting Information -

Ji-Hoon Kang [a,*], **Junghee Ryu Lee** [a], **and Hoon Ryu** [a,*,‡]

[a] *Div. of National Supercomputing, Korea Institute of Science and Technology Information, Daejeon 34141, Republic of Korea.*

[*] *These authors equally contributed.*

[‡] *Corresponding Author. E-mail: elec1020@kisti.re.kr*

1. Electronic structure simulations

Since quantum dots (QDs) are created in the 8nm-thick middle Si layer (see Figure 1(b) of the main manuscript), spatial distributions and energetic positions of confined electrons must be solved quantum mechanically. As we addressed in the Methods section of the main manuscript, the electronic structure of this middle Si layer is described with an effective mass theory where in principle the *E-k* relationship of sub-band dispersions is parabolic. The six valleys existing in the bulk Si conduction bandstructure have an effective mass of $0.92m_0$ along the longitudinal direction and $0.19m_0$ along the two transverse directions, where m_0 is the mass of an electron (9.1×10^{-31} kg). The entire set of electron energy-levels, therefore, can be obtained by solving three Schrödinger equations (one using a longitudinal effective mass and the other two using a transverse effective mass) and merging their solutions. But here we only focus on the ground state of each QD, and therefore calculate the lowest two (four with Zeeman-splitting) energy-levels of the system by solving a Schrödinger equation that uses the longitudinal mass ($0.92m_0$). The solution perfectly covers lowest energy-levels of our interest as the longitudinal mass is much heavier than the transverse one.

Normally, the single-band effective mass model is rarely used to predict the valence bandstructure of cubic semiconductors, because the simple model lacks the ability to explain

the experimentally understood complicated pattern of non-parabolicities and masses of heavy-hole, light-hole, and particularly spin-orbit split-off sub-bands. Also, all we care in this work are the energetic position and the spatial distribution of (confined) conduction electrons that are injected from the external electron reservoir, not the valance bandstructure. As a result, here we only include the conduction bandstructure to the modeling scope, and the spin-orbit coupling term is not taken into account. Finally, the Zeeman-energy term is included by using a 2×2 matrix for description of a single grid point in the simulation domain, where the two diagonal components of the matrix indicate up-spin & down-spin onsite energy at a single grid point. It is worthwhile to note our model becomes conceptually equal to the 2×2 term (representing the conduction bandstructure) of an 8-band $k \cdot p$ model [S1].

As we addressed in the main manuscript with the numerical process in Figure 1(c), the charge (electron) distribution is determined self-consistently, and the confinement pattern of electrons in the middle Si-layer (QD regions) is solely determined with this charge distribution that is obtained with the solutions (electron wavefuctions) of the Schrödinger equation. Figure S1(a), for instance, shows the distribution of electron densities at the lowest two energy-levels that are obtained at V_R = 545mv and V_L = 535mV (indicated by the red arrow in Figure 3(a) of the main manuscript), where the charge density develops around the right QD. Since the ground state energy-level at this bias conduction touches the Fermi-energy that is fixed by the external electron reservoirs, we know the only right QD is filled with an electron. As another example, Figure S1(b) shows the electron distribution at the lowest two energy-levels that are obtained at V_R = 555mv and V_L = 546mV (the yellow arrow in the Figure 3(a) of the main manuscript), which is seen by the second-injected electron. Since the ground state (where the charge density develops around the left QD) touches the Fermi-energy at this bias point, we know the left QD starts to be filled, and the system is initialized at the (1,1) charge state.

2. Modeling of the charge stability diagram

In the experimental work (Ref. [8] of the main manuscript), the charge occupancy of the double-QD system is detected by monitoring the current flowing through the adjacent QD (a charge sensor). Instead of including the charge sensor in the simulation domain, this work models the charge stability with the ballistic quantum conductance (G) that can be analytically calculated using Eq. (S1):

$$G = \frac{q^2}{h} \frac{1}{1 + e^{(E-E_F)/kT}},$$
(S1)

where q^2/h is the quantum conductance of a single electron in the ballistic regime, and the rest term is the Fermi-Dirac function that explains the occupancy of QD energy-level (E, obtained with electronic structure simulations) with respect to the Fermi-energy (E_F, grounded by the electron reservoirs). Note that the following two things are assumed: (1) Electron transport in the middle Si layer is ballistic (equivalent to assume that the effect of phonon scattering is weak in extremely low temperature and that the scattering of Si/SiGe interface roughness would not be dominant at 8nm width), and (2) E_F is constant in the middle Si layer (can be fair enough as extremely low biases are applied along the transport direction). The full charge stability diagram in Figure 3(a) of the main manuscript is obtained by calculating the derivatives of conductance within the selected ranges of top gate biases.

3. ESR frequency, exchange interaction, and valley-splitting energy

To present more detailed information than what is graphically delivered with Figure 4(c) and 4(d) of the main manuscript, we show numerical values of the variation of E_{ZL} & E_{ZR} (Figure 4(c) and J (Figure 4(d)) as a function of V_M (ranging from 395mV to 405mV with a 1mV step) in Table S1, where variations with respect to the reference case ($V_R=V_L=555$mV & $V_M=400$mV) are expressed as real values and percentiles in the top and bottom sub-table, respectively. The information delivered with Figure 5(c) of the main manuscript is also numerically presented in

Table S2 and S3, which show the values on the two central axes as a function of V_L and V_R, respectively (both V_L and V_R range from 550mV to 560mV with a 1mV step). Note that, here variations with respect to the reference case ($V_R=V_L=555$mV & $V_M=400$mV: the central point in Figure 5(c) of the main manuscript) are expressed as real values and percentiles in the top-right and bottom-right sub-table, respectively. Values of the valley-splitting energy, which can be extracted with difference of energetic position between the lowest two energy-levels under zero Zeeman-splitting of the DQD structure, *i.e.*, the ground state of the left QD and right QD, are also given in the top-left sub-table of Table S2 and S3.

References

[S1] T. B. Bahder, *Physical Review B,* 1990, *41*, 11992-12001.
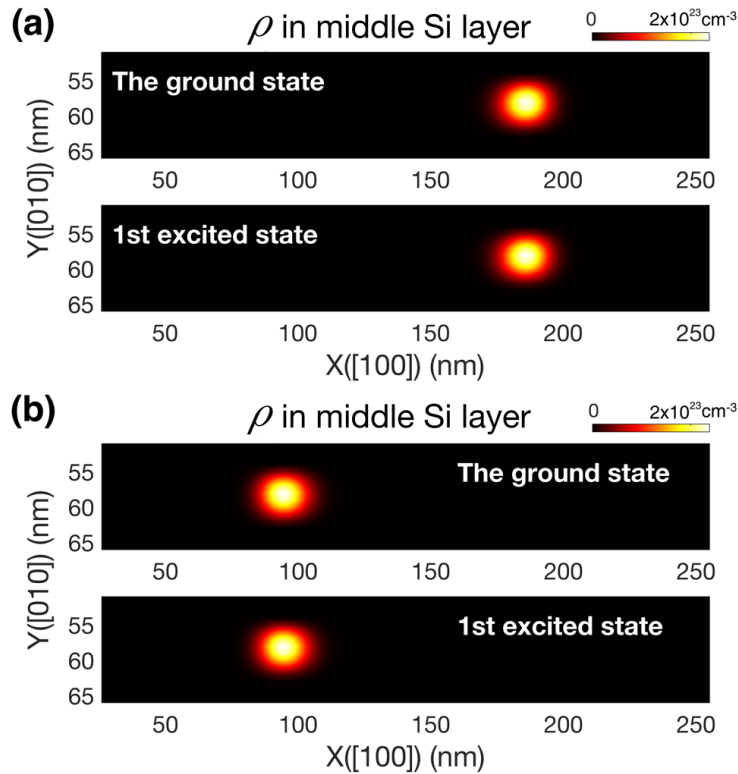
Figure S1. Spatial distribution of electrons in the middle Si layer at the lowest two energy-levels. (a) The distribution seen by the first-injected electron at $V_R = 545$mv and $V_L = 535$mV. The ground state is split into two states due to the Zeeman-splitting. (b) The distribution seen by the second-injected electron at $V_R = 555$mv and $V_L = 546$mV. In this bias conduction, the right QD is already filled with the first-injected electron.
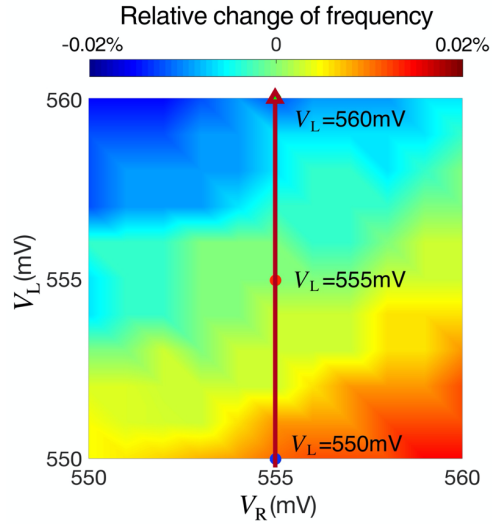
Table S1. ESR frequency (*Ez*) and exchange interaction (*J*). Changes of ESR frequency and exchange energy (with respect to the reference case: $V_L = V_R = 555mV$ & $V_M = 400mV$) are presented as a function of V_M. The upper and lower sub-table show the real value and percentile, respectively.

V_M (mV)	ΔE_{ZL} (MHz)	ΔE_{ZR} (MHz)	ΔJ (MHz)
395	–1.179	1.210	–0.109
396	–0.965	0.967	–0.105
397	–0.723	0.726	–0.098
398	–0.482	0.484	–0.084
399	–0.241	0.244	–0.056
400	0	0	0
401	0.238	–0.242	0.111
402	0.481	–0.487	0.329
403	0.724	–0.725	0.761
404	0.964	–0.965	1.612
405	1.180	–1.219	3.287

V_M (mV)	ΔE_{ZL} (%)	ΔE_{ZR} (%)	ΔJ (%)
395	–0.01466	0.01488	–96.7
396	–0.01200	0.01189	–95.8
397	–0.00899	0.00893	–87.2
398	–0.00599	0.00595	–74.6
399	–0.00300	0.00300	–49.6
400	0	0	0
401	0.00299	–0.00298	98.5
402	0.00598	–0.00599	292.0
403	0.00900	–0.00889	675.3
404	0.01198	–0.01186	1428.8
405	0.01467	–0.01499	2919.6

Table S2. ESR frequency (E_z) and valley-splitting energy as a function of V_L. Changes of ESR frequency (with respect to the reference case: $V_L = V_R = 555$mV & $V_M = 400$mV) along the middle vertical axis in Figure 5(c) of the main manuscript are shown in the top-right (real value) and bottom-right sub-table (percentile). Values of the valley-splitting energy are also shown in the bottom-left sub-table.


V_L (mV)	ΔE_{ZL} (MHz)	ΔE_{ZR} (MHz)
550	1.043	0.483
551	0.724	0.350
552	0.531	0.241
553	0.326	0.169
554	0.145	0.077
555	0	0
556	–0.167	–0.072
557	–0.339	–0.152
558	–0.555	–0.220
559	–0.876	–0.314
560	–1.279	–0.471

V_L (mV)	Valley-splitting energy (eV)
550	9.94×10^{-4}
551	7.95×10^{-4}
552	5.97×10^{-4}
553	3.98×10^{-4}
554	1.99×10^{-4}
555	5.00×10^{-10}
556	2.00×10^{-4}
557	4.01×10^{-4}
558	6.01×10^{-4}
559	8.02×10^{-4}
560	1.00×10^{-3}

V_L (mV)	ΔE_{ZL} (%)	ΔE_{ZR} (%)
550	0.01296	0.00593
551	0.00900	0.00430
552	0.00660	0.00297
553	0.00405	0.00208
554	0.00180	0.00095
555	0	0
556	–0.00207	–0.00089
557	–0.00421	–0.00187
558	–0.00690	–0.00270
559	–0.01089	–0.00386
560	–0.01590	–0.00579

Table S3. ESR frequency (*Ez*) and valley-splitting energy as a function of *V*_R. Changes of ESR frequency (with respect to the reference case: $V_L = V_R = 555\text{mV}$ & $V_M = 400\text{mV}$) along the middle lateral axis in Figure 5(c) of the main manuscript are shown in the top-right (real value) and bottom-right sub-table (percentile). Values of the valley-splitting energy are also shown in the bottom-left sub-table.
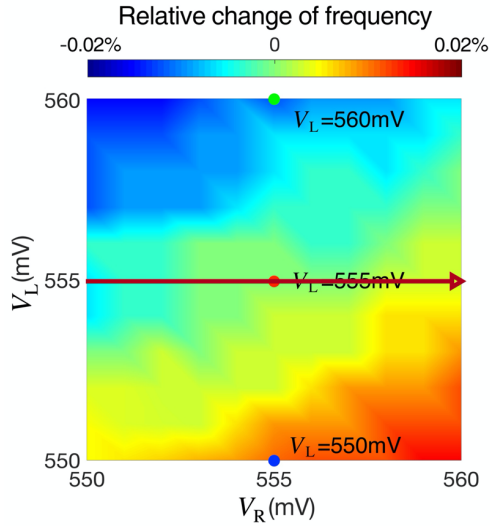
V_R (mV)	ΔE_{ZL} (MHz)	ΔE_{ZR} (MHz)
550	–0.796	–0.893
551	–0.505	–0.555
552	–0.314	–0.370
553	–0.188	–0.185
554	–0.105	–0.072
555	0	0
556	0.106	0.097
557	0.191	0.241
558	0.362	0.483
559	0.507	0.724
560	0.724	0.965

V_R (mV)	Valley-splitting energy (eV)
550	9.94×10^{-4}
551	7.95×10^{-4}
552	5.97×10^{-4}
553	3.98×10^{-4}
554	1.99×10^{-4}
555	5.00×10^{-10}
556	2.00×10^{-4}
557	4.01×10^{-4}
558	6.01×10^{-4}
559	8.02×10^{-4}
560	1.00×10^{-3}

V_R (mV)	ΔE_{ZL} (%)	ΔE_{ZR} (%)
550	–0.00990	–0.01098
551	–0.00628	–0.00682
552	–0.00390	–0.00455
553	–0.00234	–0.00227
554	–0.00130	–0.00089
555	0	0
556	0.00132	0.00119
557	0.00237	0.00297
558	0.00450	0.00593
559	0.00630	0.00890
560	0.00900	0.01187